TU Delft

Delft University of Technology

Document Version
Final published version

Licence
Dutch Copyright Act (Article 25fa)

Citation (APA)
Nguyen-Minh, T., & Kestens, L. A. I. (2026). On the Rotated Cube 001110 Texture Component in Extra and Ultra Low-Carbon Steels. *Metallurgical and Materials Transactions A: Physical Metallurgy and Materials Science*. https://doi.org/10.1007/s11661-026-08196-x

Important note
To cite this publication, please use the final published version (if applicable).
Please check the document version above.

Copyright
In case the licence states “Dutch Copyright Act (Article 25fa)”, this publication was made available Green Open Access via the TU Delft Institutional Repository pursuant to Dutch Copyright Act (Article 25fa, the Taverne amendment). This provision does not affect copyright ownership.
Unless copyright is transferred by contract or statute, it remains with the copyright holder.

Sharing and reuse
Other than for strictly personal use, it is not permitted to download, forward or distribute the text or part of it, without the consent of the author(s) and/or copyright holder(s), unless the work is under an open content license such as Creative Commons.

Takedown policy
Please contact us and provide details if you believe this document breaches copyrights.
We will remove access to the work immediately and investigate your claim.

This work is downloaded from Delft University of Technology.

On the Rotated Cube ($\{001\}\langle 110\rangle$) Texture Component in Extra and Ultra Low-Carbon Steels

T. NGUYEN-MINH and L.A.I. KESTENS

Crystallographic texture plays a central role in determining the mechanical and functional properties of low-carbon steel sheets. While the γ-fiber ($\langle 111\rangle//ND$) texture has been extensively studied and effectively controlled through conventional rolling and annealing routes, the Cube ($\langle 001\rangle//ND$) fiber, particularly the Rotated Cube ($\{001\}\langle 110\rangle$) component, remains poorly understood and rarely exploited, despite its potential benefits for soft magnetic applications. This manuscript reviews and rationalizes the formation and evolution of the Rotated Cube texture obtained through conventional sheet processing, encompassing phase transformation, cold rolling, and recrystallization annealing. Experimental observations demonstrate that the Rotated Cube component is continuously present, albeit with comparatively low intensities, because (extra/ultra) low-carbon steels have historically been optimized to suppress its development. The evolution of the Rotated Cube texture cannot be explained solely by classical orientation stability or high stored energy recrystallization arguments. Instead, evidence points to the decisive role of variant selection during the $\gamma \rightarrow \alpha$ transformation, grain fragmentation during plastic deformation, and orientation selection during sub-grain growth, controlled by local misorientation gradients, in the early stages of recrystallization annealing. The manuscript further evaluates the capabilities and limitations of mean-field and full-field computational approaches for texture prediction, highlighting recent advances that incorporate microstructural heterogeneity into recrystallization modeling. By integrating experimental findings with physically based models, this work clarifies the multiscale mechanisms underlying Rotated Cube texture formation and outlines pathways toward its intentional control in low-carbon steels processed *via* conventional routes.

https://doi.org/10.1007/s11661-026-08196-x
© The Minerals, Metals & Materials Society and ASM International 2026

I. INTRODUCTION

POLYCRYSTALLINE metals and alloys frequently exhibit a crystallographic texture, which is reminiscent of the physical processes underlying microstructural formation during thermomechanical processing. Texture development in the subsequent stages of hot/cold rolling and annealing is well documented and the natural tendency is to develop a strong γ-fiber ($\langle 111\rangle//ND$) on the finished product, particularly for extra- and ultra-low-carbon steels, with less than 0.050 and 0.010 wt pct C, respectively. It is well-known that the γ-fiber provides excellent deep-drawing properties to such extra-/ultra-low-carbon steels and there is plenty of literature reports on the physical mechanisms enhancing the γ-fiber steel texture. Apart from the γ-fiber texture, there's also abundant interest in the development of the Goss texture ($\{110\}\langle 001\rangle$), which is optimally suited for Grain Oriented (GO) electrical steel, used as magnetic flux carrier in transformers. There is a decades long very lively scientific debate, not yet fully resolved, on the origin of the Goss texture component appearing during secondary recrystallization in the finishing annealing treatment of GO electrical steel.

However, comparatively little attention has been devoted to enhancing the development of the Rotated Cube texture component ($\{001\}\langle 110\rangle$) in low-carbon steels, although this component is of crucial importance for the magnetic quality of Non-Oriented (NO) electrical steel, which is extensively used as ferromagnetic core for a wide variety of rotating electromagnetic devices.[1] Given the growing importance of such electromagnetically driven machines, the aim of this work is to

T. NGUYEN-MINH is with the Materials Science and Technology Group, Department of Electromechanical, Systems and Metal Engineering, Ghent University, Tech Lane Ghent Science Park 46, Zwijnaarde, B9052 Ghent, Belgium. L. A. I. KESTENS is with the Materials Science and Technology Group, Department of Electromechanical, Systems and Metal Engineering, Ghent University and also with the Department of Materials Science and Engineering, Delft University of Technology, Mekelweg 2, 2628CD Delft, The Netherlands. Contact e-mail: Leo.Kestens@UGent.be.
Manuscript submitted January 14, 2026; accepted March 6, 2026.

Published online: 23 March 2026

rationalize the formation and evolution of the Rotated Cube texture component in low-carbon steel during flat-sheet processing. Experimental evidence for the appearance and evolution of the Rotated Cube component during phase transformation after hot rolling, plastic deformation during cold rolling, and recrystallization annealing is reviewed. Hence, we limit ourselves here to the rolling of low-carbon steels with BCC crystal structure at room temperature and a fully FCC austenite structure above the A3 temperature. This is followed by a discussion of the underlying mechanisms governing texture development from the perspective of physically based models. Finally, a summary and outlook are provided, addressing the challenges and opportunities associated with Cube texture control in low-carbon steels processed *via* conventional routes.

II. EXPERIMENTAL OBSERVATIONS

Figure 1 shows the crystallographic textures of typical low-carbon steel products following conventional rolling and annealing processes. In the $\varphi_2 = 45$ deg ODF sections, the intensity of the Rotated Cube texture component is relatively weak compared to the $\gamma - (\langle 111\rangle//ND)$, the $\alpha - (\langle 110\rangle//RD)$, and the $\alpha^* - (\{hh1\}\langle 21h\rangle)$ fiber intensities. Such observations may give the impression that the development of the Rotated Cube texture is not intrinsically enhanced by conventional rolling and annealing, and its control through conventional sheet manufacturing routes is infeasible. However, it should be noted that the current configuration and parameters of industrial rolling and annealing lines have been deliberately designed and optimized to suppress the formation of the Rotated Cube component texture on the final product, rather than promote it. This section reviews the key physical phenomena associated with the individual steps of conventional sheet manufacturing, with particular emphasis on the presence and evolution of the Rotated Cube texture component after each processing stage. These experimental observations serve as the basis for subsequent discussion of the formation mechanism(s) of the Rotated Cube texture component presented in the following section.

A. *Phase Transformation Textures*

Iron and low-carbon steels are allotropic materials that exhibit two crystallographic structures: body-centered cubic (BCC) at room temperature and face-centered cubic (FCC) at elevated temperatures. The transformation between these two cubic structures proceeds through atomic rearrangements across the interphase boundary, occurring *via* either diffusional or displacive mechanisms. During this phase transformation, the crystallographic orientations of the product phase are commonly inherited from those of the parent phase through well-defined orientation relationships (ORs) between the two crystal structures. Among these, the Kurdjumov–Sachs (K–S),[2] Nishiyama–Wasserman (N–W),[3] and Greninger–Troiano (G–T)[4] relationships are the most widely recognized ORs between the BCC (α) and FCC (γ) phases in iron and low-carbon steels. These ORs are illustrated in Figure 2 by the {001} pole figure, which depicts the orientations of a Cube ($\{001\}\langle 100\rangle$) austenite grain and its corresponding ferrite transformation products. Differences among the ORs, which give rise to distinct sets of ferrite variants, are commonly attributed to variations in the α–γ interfacial energy arising from changes in chemical composition. Notably, the {001} pole figure also reveals a direct correspondence between the Cube austenite texture and its nearly Rotated Cube ferrite variants, irrespective of whether the transformation follows the K–S, N–W, or G–T orientation relationship.

The presence of the Rotated Cube texture in hot rolled and annealed dual phase (DP) steels, as shown in Figure 3(a), is commonly attributed to the transformation of Cube oriented austenite grains. However, the Rotated Cube orientation is not the sole transformation product of the austenite Cube component, due to the high crystallographic symmetry of both the BCC and FCC structures. In the absence of variant selection during the $\gamma \rightarrow \alpha$ phase transformation, the texture intensity associated with the Rotated Cube orientation is

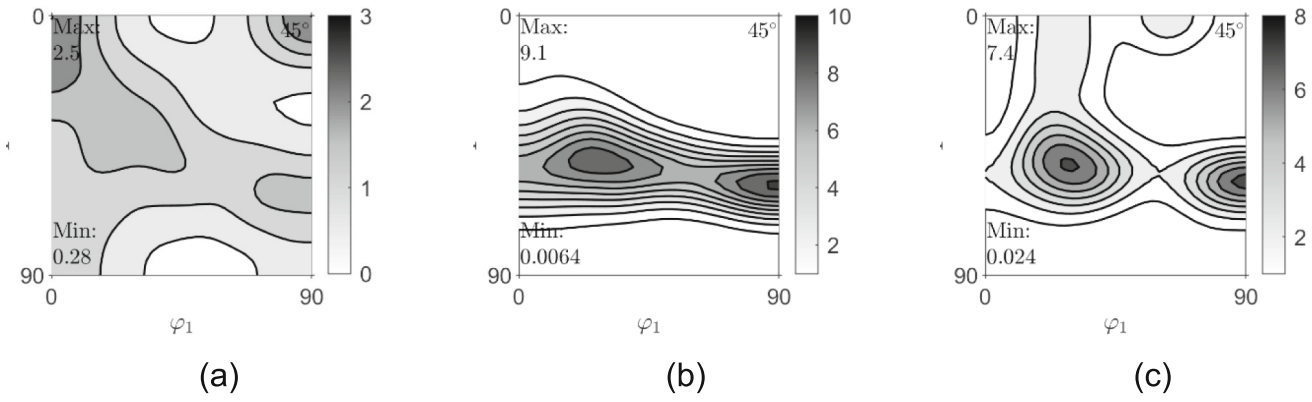


Fig. 1—Crystallographic textures given by $\varphi_2 = 45$ deg ODF sections of (*a*) hot rolled and annealed, (*b*) cold rolled and annealed Interstitial Free (IF) steels, and (*c*) cold rolled and annealed Non-Oriented (NO) electrical steel.

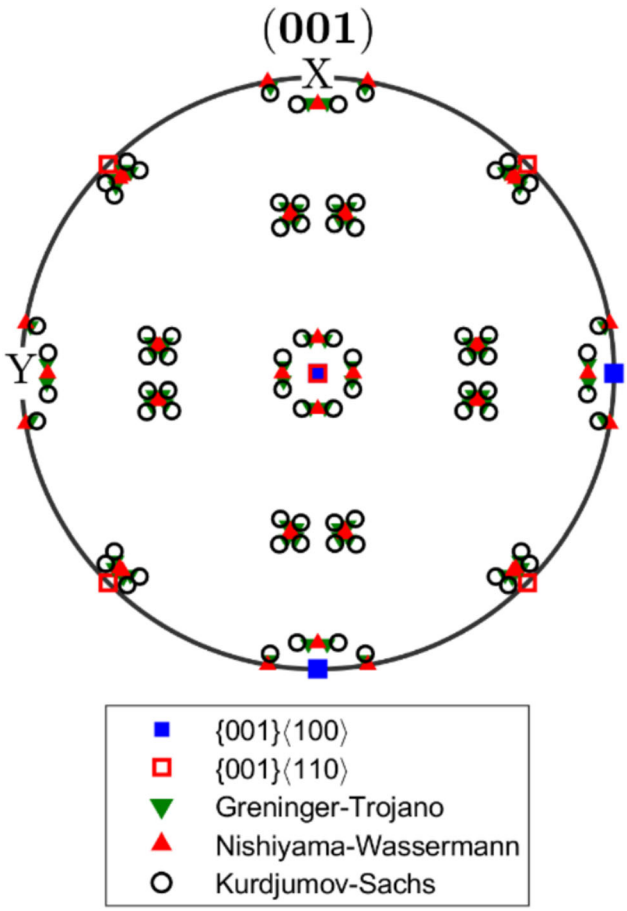


Fig. 2—The {001} pole figure of a Cube oriented austenite grain and its transformation variants according to the K–S, N–W, and G–T orientation correspondences.

expected to be at least a factor of two lower than that of the parent Cube orientation, owing to the concurrent formation of Goss and Rotated Goss ($\{110\}\langle 110\rangle$) variants, as also illustrated in Figure 3(a). When the same material is annealed at 950 °C for 1 hour under the vacuum an interesting development of the transformation texture as given in Figure 3(b) is observed. The texture intensity of 12 times the random level measured near the Rotated Cube component exposes a strong and intricate variant selection rule during the α–γ–α phase transformation. Though the formation of this Rotated Cube texture can be partially attributed to the effects of chemical composition on the steel surface energy[5–7] quantitative arguments for this variant selection mechanism remain largely unknown.

B. *Cold Rolling Textures*

Cold rolling deformation is widely recognized as the primary mechanism responsible for the development of $\alpha\,(\langle 110\rangle//RD)-$ and $\gamma\,(\langle 111\rangle//ND)$-fiber textures in BCC materials. In iron and low-carbon steels, moderate cold rolling with thickness reductions of approximately 65 to 85 pct typically leads to a pronounced α-fiber ($\langle 110\rangle//RD$) texture, with the highest intensity commonly located near the $\{112\}\langle 110\rangle$ component, as illustrated in Figure 4. The Rotated Cube orientation, which also belongs to the α-fiber, is present in these deformation textures (*cf.* Figure 4). However, its intensity is generally lower than that of the $\{112\}\langle 110\rangle$ component.

Based on considerations of orientation stability (*cf.* Figure 7) under plane-strain compression, the Rotated Cube orientation would be expected to become less

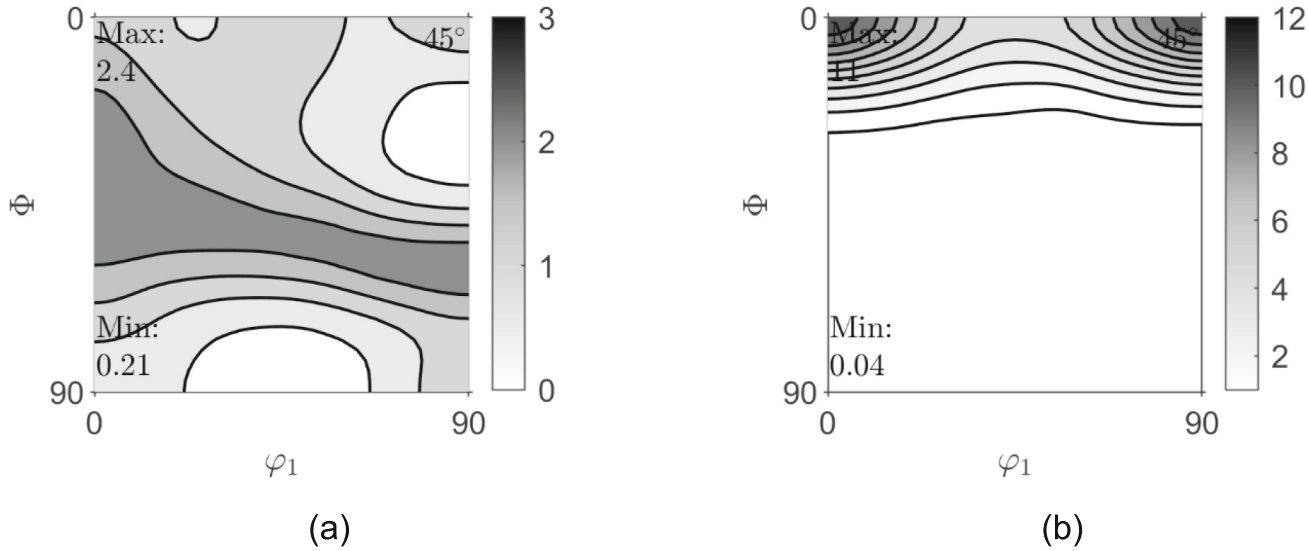


Fig. 3—The $\varphi_2 = 45$ deg ODF section of the transformation textures in a hot rolled and annealed DP steel (*a*) before and (*b*) after the vacuum annealing at 950 °C for 1 h.

favorable with increasing rolling reduction, for example in the range of 85 to 95 pct, owing to its lower stability compared with the {112}⟨110⟩ and the {111}⟨112⟩ orientations. Contrary to this expectation, the deformation texture of a Fe–2.8 wt pct Si alloy subjected to 85 pct cold rolling reduction [*cf.* Figure 5(a)] exhibits an enhanced Rotated Cube texture component, which becomes increasingly pronounced with increasing strain. This behavior is not an isolated observation, because similar strengthening of the Rotated Cube texture has also been reported for low-carbon steels subjected to heavy cold rolling with thickness reductions of up to 95 pct and more.[8–10]

While the enhancement of the Rotated Cube texture as a result of heavy cold rolling cannot be explained by considerations of orientation stability alone, maintaining the stability of this orientation under varying rolling conditions has been shown to increase the volume fraction of the Rotated Cube component in the deformation texture.[11] Cross rolling, in which the rolling direction in each subsequent passes is rotated by 90 deg relative to the preceding pass, successfully developed a sharp Rotated Cube texture with intensities of approximately 130 to 150 multiples of a random distribution (m.r.d.) in low-carbon steel sheets subjected to a total thickness reduction of 70 pct. By alternating the rolling and transverse directions between successive rolling passes, the stability of most α-fiber texture components, except for the Rotated Cube orientation, is reduced, leading to preferential reorientation toward the Rotated Cube component (*cf.* Figure 6).

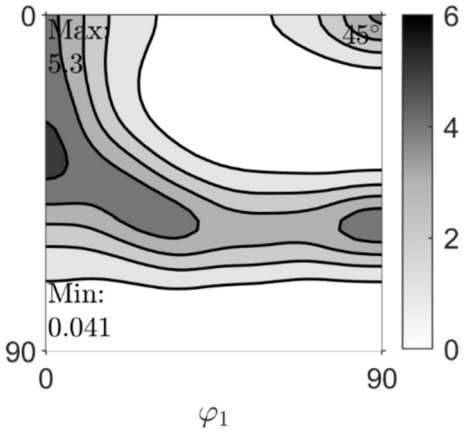
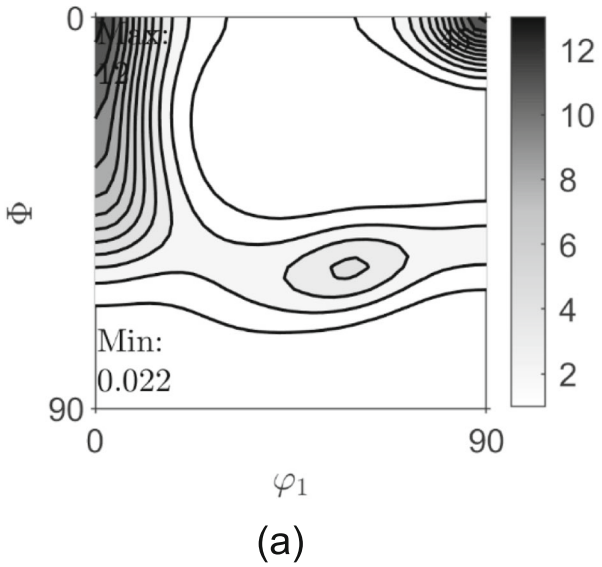


Fig. 4—The $\varphi_2 = 45$ deg ODF section shows texture of an IF steel sample after 75 pct cold rolling.

C. *Recrystallization Textures*

Recrystallization is the restoration of deformed grains to a comparatively defect-free state through the migration of high angle grain boundaries driven by gradients in stored plastic energy. During recrystallization, grains that accumulate less strain energy and have larger size will grow preferentially. Because there is considerable variation in how crystals of different orientations locally accommodate the boundary conditions of the macroscopically imposed displacement field, both sub-grain size and stored energy are expected to be functions of crystallographic orientation. These substructural intricacies of the deformation give rise to preferential nucleation and growth of the γ-fiber during recrystallization in iron and low-carbon steels, as illustrated in Figure 1.

The apparent absence of the Rotated Cube component from the recrystallization textures of cold rolled and annealed low-carbon steels (*cf.* Figure 1) is commonly attributed to its comparatively low stored energy, which limits its ability to enhance the nucleation process



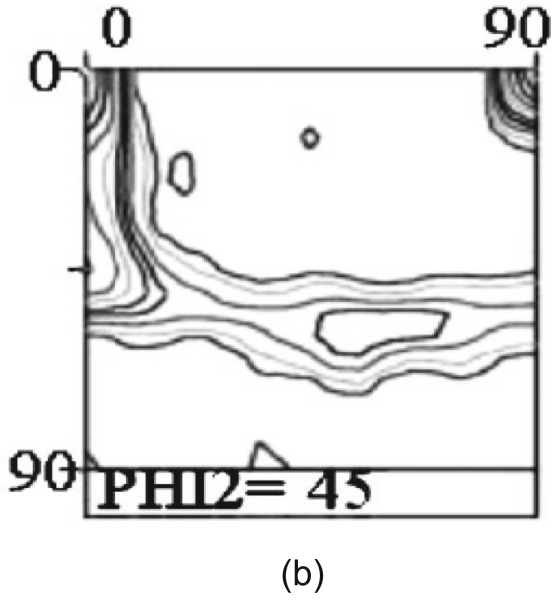


Fig. 5—Deformation textures represented by the $\varphi_2 = 45$ deg ODF sections for (*a*) an NO electrical steel after the cold rolling of 85 pct thickness reduction and (*b*) an IF steel after the cold rolling of 99.9 pct thickness reduction, adapted from this figure of Ref. [8].

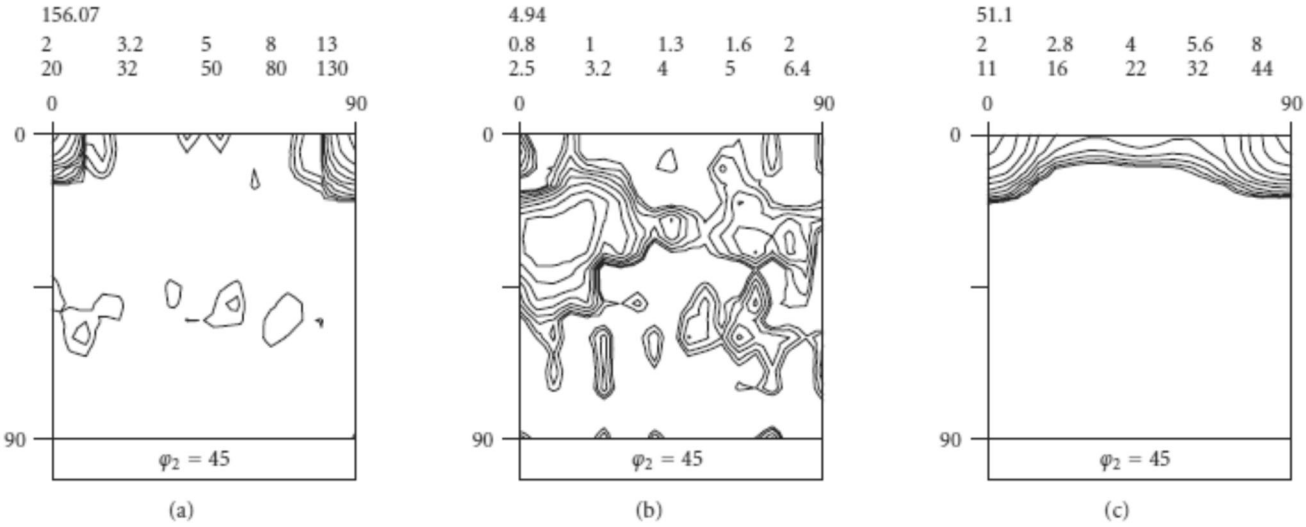


Fig. 6—Textures observed after (*a*) cross rolling, (*b*) primary recrystallization annealing and (*c*) after a skin rolling pass of 8 pct thickness reduction and additional annealing treatment, adapted from Fig. 7 of Ref. [12].

during recrystallization. This, however, does not imply that $\langle 111\rangle//ND$-oriented grains completely consume the Rotated Cube grains present in the deformation microstructure. Instead, α*-fiber texture components, most notably the $\{311\}\langle 136\rangle$ orientation, have been proposed as recrystallization products originating from Rotated Cube grains and other $\langle 110\rangle//RD$ fiber components.[8,10,11,13,14] Although the mechanisms governing the formation of the $\{hh1\}\langle 21h\rangle$ orientations in low-carbon steels following severe cold rolling and annealing remain incompletely understood, their direct link to the α-fiber deformation texture is well established.

In processing conditions whereby the γ-fiber texture is suppressed, the growth of the Rotated Cube orientation and related texture components, such as $\{311\}\langle 136\rangle$ and Cube $\{001\}\langle 100\rangle$, has been observed.[8,11] For example, cross rolling effectively weakens the γ-fiber in the deformation microstructure and promotes the development of $\{hh1\}\langle 21h\rangle$ primary recrystallization textures.[15] Similarly, the combination of a light skin-pass rolling (4 to 8 pct thickness reduction) followed by recrystallization annealing has been shown to produce a pronounced Cube fiber, with Rotated Cube intensities reaching approximately 50 multiples of a random distribution (m.r.d.) in low-carbon steel sheets.[12] Additionally, the growth of Cube ($\{001\}\langle 100\rangle$)-oriented grains, rarely observed after conventional cold rolling and annealing, was first predicted and subsequently observed within micro-shear bands of Rotated Goss ($\{110\}\langle 110\rangle$) crystals.[16,17]

Collectively, these observations demonstrate that the development of Rotated Cube grains during conventional sheet manufacturing is more complex than the well-established evolution of the γ-fiber texture. To fully rationalize the presence and evolution of the Rotated Cube texture in conventionally processed steel sheets, a theoretical framework based on physically informed models is therefore required. Such models are essential for rationalizing the emergence of Rotated Cube textures under conventional thermomechanical paths and for guiding texture design in low-carbon steels processed *via* advanced manufacturing.

III. PHYSICALLY BASED MODELS

Because crystallographic texture is an integral part of the metallic microstructure, any crystallographically resolved microstructure model can, in principle, be employed to simulate texture formation and evolution during metallurgical processes. However, as texture is inherently a statistical property, reliable texture evolution modeling typically requires the sampling of several thousands of crystallographic orientations. Because this number of variables is computationally challenging, crystallographic texture is quantitatively described by an orientation distribution function (ODF) rather than a scalar quantity, rendering texture evolution a high-dimensional problem analogous to an *n*-body system. Depending on the number of state variables considered and the objectives of the simulation, computational microstructure approaches are commonly categorized into two classes: full-field and mean-field models.

In full-field microstructural models the state variables are space and time resolved to obtain a full topological description of the system as a function of time. Microstructural evolution associated with phase transformation, crystal plasticity, and (sub-)grain growth has been successfully simulated using approaches such as cellular automata (CA),[18] Monte Carlo (MC),[19,20] crystal plasticity finite element (CPFE),[21,22] and crystal plasticity fast Fourier transform (CPFFT)[23,24] methods. Provided that an accurate representation of the

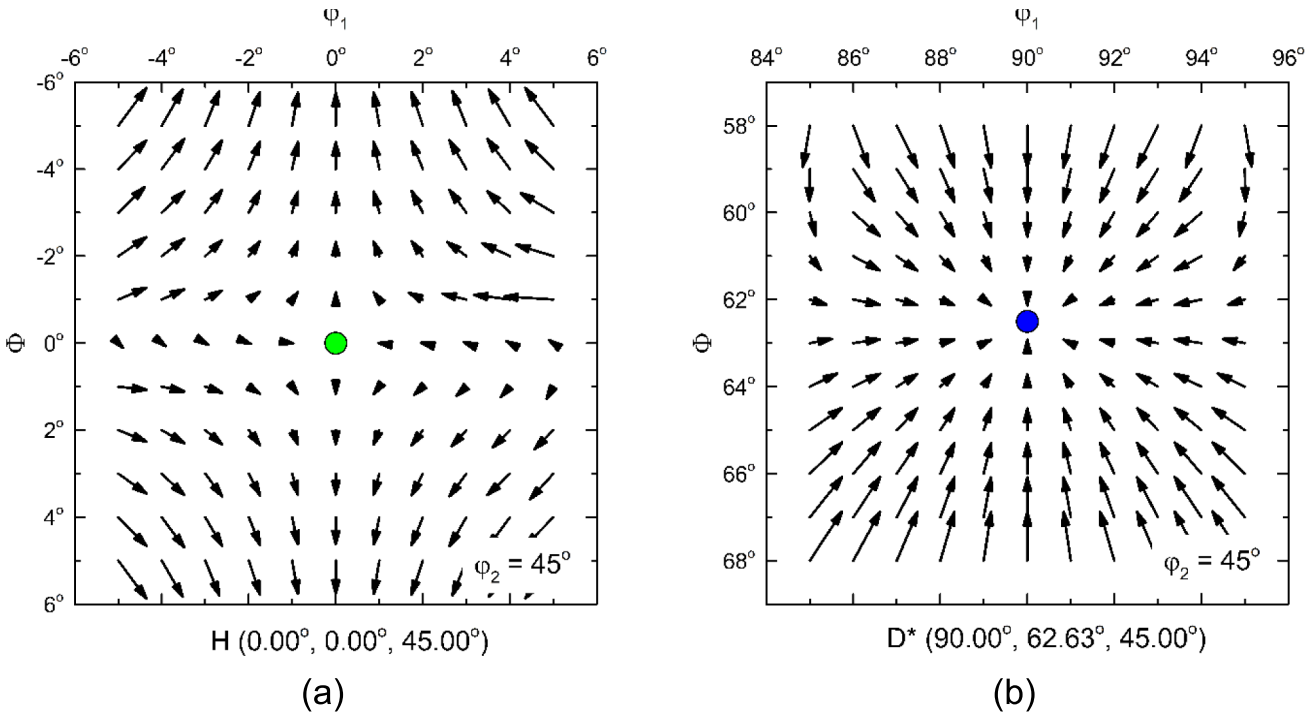


Fig. 7—The rotation fields near (*a*) the {001}⟨110⟩, (*b*) the {111}⟨112⟩ orientations calculated by the FCT model for BCC materials under the plane strain compression.

initial microstructure (*i.e.*, a representative volume element, RVE) is employed, full-field models can capture texture evolution in low-carbon steels with high fidelity. However, the high computational cost and the limited number of crystallographic orientations that can be practically represented remain major limitations of full-field approaches. These constraints are particularly critical for phase-field (PF) models when applied to texture evolution simulations.

In contrast, mean-field models represent the microstructure using statistical state variables, and microstructural evolution is described by the numerical solution of differential equations governing the response of these variables to external boundary conditions. Although mean-field approaches lack the explicit topological resolution inherent to full-field models, they offer several advantages that are particularly well suited for texture studies. In general, mean-field models require significantly lower computational resources than full-field approaches, making them more amenable to industrial-scale applications. Moreover, owing to its inherently statistical nature, crystallographic texture can be modeled independently of other microstructural features within a mean-field framework.

In this study, although texture evolution is the primary focus, the physical mechanisms underlying texture formation necessitate consideration of both statistical and spatial aspects of the microstructure. Accordingly, a combination of mean-field and full-field computational approaches is explored to analyze the formation and evolution of the Rotated Cube texture in low-carbon steels.

A. *Transformation Texture Simulations*

Phase transformations in metals have been extensively studied from a variety of perspectives, both with full- and mean-field modeling approaches for the $\alpha \leftrightarrow \gamma$ transformation in low-carbon steels. Full-field models, such as cellular automata (CA) and phase-field (PF) methods, typically describe solid-state phase transformations and solidification from a chemical, thermodynamic, and kinetic standpoint.[25,26] In these models, crystallographic and micromechanical aspects are rarely the primary focus. Although efforts have been made to incorporate crystallographic features into full-field phase transformation models,[27–29] existing simulations are largely restricted to mono- or oligo-crystalline anisotropy rather than capturing orientation-dependent behavior in truly polycrystalline aggregates.

In contrast, relatively simple mean-field approaches can predict transformation textures from parent textures with reasonable accuracy. By applying crystallographic rotations defined by specific orientation relationships (*e.g.*, Kurdjumov–Sachs, Nishiyama–Wasserman, or Greninger–Troiano) to ensembles of several thousand discrete orientations, mean-field models can effectively simulate texture evolution during phase transformation. More advanced formulations represent both orientation relationships and textures using probability density functions.[30–32] Consequently, mean-field simulations not only reproduce transformation textures but also provide insight into variant selection mechanisms operative during the phase transformation.

Variant selection during phase transformation can be regarded as a symmetry-breaking process driven by external or internal boundary conditions acting during

nucleation of the new phase. Among the various microstructural features of the parent phase, grain boundaries constitute the most favorable nucleation sites owing to the reduction in activation energy when the phase transformation is initiated at a grain boundary of the parent phase. This energy is further reduced when a nucleus satisfies a double Kurdjumov–Sachs (K–S) orientation relationship with both adjacent parent grains.[33,34] The observation of a double K–S orientation relation gives rise to the peculiar effect of texture memory, observed during a forward and reverse α–γ–α phase transformation, *e.g.*, occurring when a cold rolled IF steel is annealed in the full austenite domain. The texture of the parent phase may be largely retained or even enhanced rather than being weakened by cyclic thermal annealing.[35]

The presence of the Rotated Cube component in ferrite textures is readily explained when parent austenite grains undergo recrystallization prior to the $\gamma \rightarrow \alpha$ transformation. However, the pronounced enhancement of the Rotated Cube texture observed in a fully finished DP steel after annealing at 950 °C under vacuum (Figure 6) suggests that additional mechanisms are operative, pointing not to experimental artifacts but to variant selection effects during phase transformation. Addressing this issue requires improved predictive capability in both mean-field and full-field phase transformation models. For example, extending mean-field approaches to incorporate additional statistical descriptors beyond orientation and boundary distribution functions would broaden their applicability beyond texture prediction alone and enable a more comprehensive description of variant selection phenomena.

B. *Deformation Texture Simulations*

1. *Mean-field crystal plasticity (CP) models*

Deformation texture simulation represents one of the most successful examples of mean-field crystal plasticity (CP) models. Originally developed to address the specific case of single-crystal plasticity under uniaxial loading,[36] mean-field CP frameworks have since been generalized to treat the more complex problem of polycrystal plasticity under arbitrary strain paths.[37,38] By invoking homogenization assumptions between macroscopic boundary conditions and individual crystal accommodation, relaxed versions of the full-constraint Taylor (FCT) model can reproduce deformation textures in both BCC and FCC materials with reasonable accuracy.[39] Far reaching simplifications that neglect singular crystal behavior during plastic deformation significantly reduce computational cost and enable simulations involving large orientation ensembles.

Even without an explicit description of strain hardening or dislocation-structure evolution, simplified formulations such as the LAMEL model have been shown to capture the deformation texture of interstitial-free (IF) steels after 70 pct cold rolling with reasonable accuracy.[40] In the context of conventional crystal plasticity models, the formation and evolution of the deformation texture in low-carbon steels under moderate cold rolling can be rationalized in terms of orientation stability. As shown in Figure 7, both the Rotated Cube ($\{001\}\langle 110\rangle$) and the $\{111\}\langle 112\rangle$ orientations exhibit zero rotation rates under plane-strain compression. The convergent nature of the rotation field surrounding the $\{111\}\langle 112\rangle$ orientation predicts a higher texture intensity of this component than of the Rotated Cube orientation as the rolling reduction increases. Texture characterization on the Fe−2.8 wt pct Si alloy sample after 85 pct thickness reduction, as given in Figure 5, however exhibits an opposing tendency.

Neglecting microstructural topology and individual crystal boundary conditions in mean-field CP models, however, introduces several limitations: (i) reduced predictive accuracy at large strains; (ii) systematic overestimation of texture intensity; (iii) artificial treatment of mechanical twinning; (iv) omission of grain fragmentation; and (v) restriction to single-phase materials. More advanced formulations, such as the viscoplastic self-consistent (VPSC) and advanced LAMEL (ALAMEL) models, address some of these shortcomings by incorporating topological features in the statistical ensemble, which is still a subject of ongoing research.[41,42] Nevertheless, the development of the Rotated Cube texture in low-carbon steels under heavy cold rolling remains beyond the predictive capability of current mean-field CP models.

2. *Full-field crystal plasticity (CP) models*

While microstructural topology is not an explicit state variable in mean-field crystal plasticity (CP) models, it plays a central role in the performance of full-field CP approaches. In the 1990 s, Taylor-type crystal plasticity was first embedded within fully implicit finite element frameworks, enabling the prediction of not only texture evolution but also local stresses, strains, and geometric changes during plastic deformation.[21] With increased integration-point density and refined time discretization, crystal plasticity finite element (CPFE) models have since been applied to increasingly complex deformation problems. By explicitly accounting for both macroscopic boundary conditions and microstructural topology, full-field CP models have demonstrated strong capability in simulating microstructure evolution with high fidelity.[22]

More recently, spectral methods based on fast Fourier transforms, in which crystal plasticity is formulated using harmonic functions, have extended full-field CP modeling to large-strain regimes and sub-grain-scale phenomena.[23,24,43] Despite these advances, high computational cost and the requirement for an accurate description of the initial microstructure remain the principal limitations of full-field CP approaches.

In a recent study,[44] deformation textures observed in a low-carbon steel subjected to 75 pct cold rolling reduction were simulated, whereby mean-field models (full-constraint Taylor, VPSC, and ALAMEL) were compared with a full-field Crystal Plasticity Fast Fourier Transform (CPFFT) prediction. With increasing plastic strain, CPFFT predictions showed an improved agreement with experimental observations compared with mean-field formulations although for small and medium

strains the mean-field models performed better in terms of texture prediction. Among the latter, the VPSC and ALAMEL models outperformed the full-constraint Taylor model owing to their partial incorporation of microstructural topology. However, the somewhat improved accuracy of the CPFFT model at the maximum rolling reduction of 75 pct comes at a considerable computational cost even to the extent that it is impractical to use such models of real-life industrial applications.

According to the current state-of-the-art the insights gained from full-field CP models, based on a crystallographically resolved description of strain hardening, are valuable for obtaining a more complete understanding of the microstructural substructure including the appearance of meso-scale features such as deformation bands, shear bands and grain fragmentation. It is particularly the absence of an accurate description of these fragmentation phenomena that limit the performance of mean-field CP models at higher strains.

C. *Recrystallization and Grain Growth Models*

Like solid-state phase transformations, recrystallization (ReX) and grain growth (GG) constitute long-standing and widely studied topics in materials science, with also modeling divided into full-field and mean-field approaches. Full-field ReX and GG models primarily focus on microstructural topology and its temporal evolution. Grain morphology and growth kinetics have been simulated with high accuracy using phase-field (PF), cellular automata (CA), and Monte Carlo (MC) methods.[19,45]

While advanced full-field ReX and GG models can resolve hundreds, and in some cases thousands of grains, the rapid growth of selected nuclei with favorable orientations severely limits the temporal and spatial scope of such simulations. In practice, full-field models typically capture only selected stages of recrystallization rather than the entire process. Moreover, a detailed and accurate description of the initial microstructure is required to ensure meaningful simulation outcomes. Consequently, except for some recent developments discussed hereunder, full-field ReX and GG models have been predominantly applied to the study of grain morphology and growth kinetics, rather than to the prediction of crystallographic texture.

Precise descriptions of initial microstructures though not mandatory may enhance the performance of the mean-field recrystallization and grain growth (ReX&GG) models. Dislocation density, as the main carrier of plastically stored energy in the deformed crystals, constitutes the primary driving force for recrystallization, and its heterogeneous distribution among differently oriented grains underlies the development of recrystallization textures in low-carbon steels. While both experimental characterization and computational prediction of dislocation density in polycrystalline materials remain challenging, estimations of this quantity have proven effective when incorporated in mean-field recrystallization texture models.

In this context, the Taylor factor derived from mean-field crystal plasticity models has been proposed as a surrogate measure of the orientation dependence of the dislocation density in deformed crystals[15] for a given velocity field. In essence the Taylor factor is a dimensionless measure of the orientation dependence the instantaneously dissipated plastic work on the active slip systems and therefore, it makes sense to assume that it is proportional to the stored energy accumulated during deformation. Consequently, grains with orientations less susceptible to accommodate the boundary conditions of the imposed velocity field are expected to

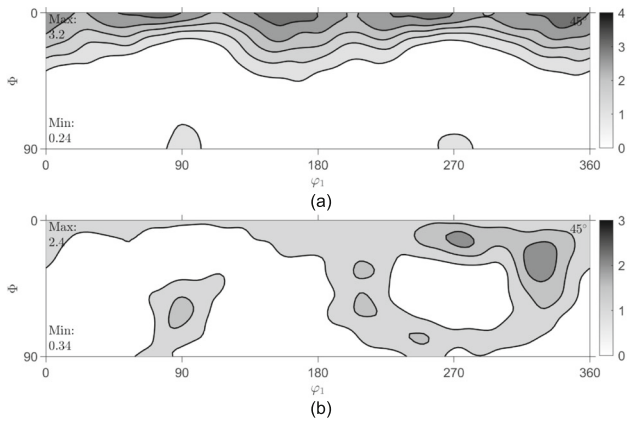


Fig. 9—Recrystallization textures in warm conventionally (*a*) and asymmetrically (*b*) rolled Fe−1.2 wt pct Si alloy after the annealing at 900 °C for 2 h.

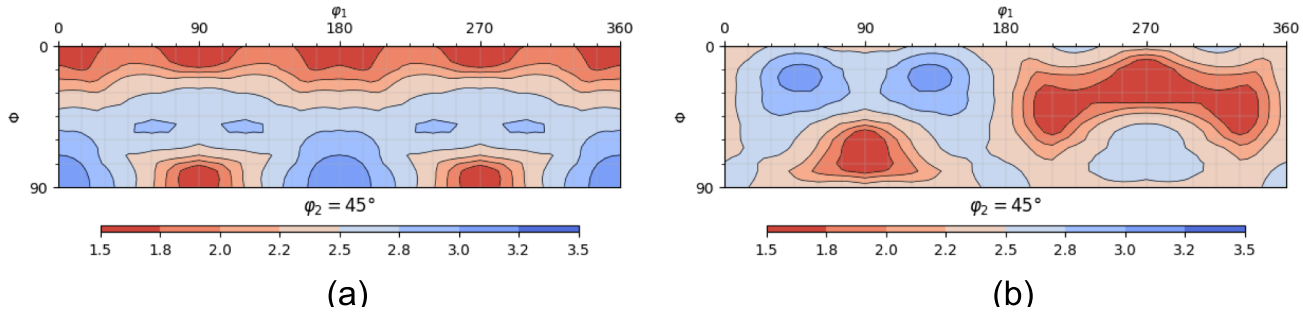


Fig. 8—Distribution of stored energy represented by Taylor factor among various oriented crystals under (*a*) conventional rolling and (*b*) asymmetric rolling deformations predicted by the FCT crystal plasticity model.

exhibit higher levels of slip activity and therefore also an increased level of stored energy, providing a crystallographic basis for the description of orientation-dependent nucleation and growth during recrystallization.[15]

In cold rolled low-carbon steels, γ-fiber grains are characterized by intense slip activity, high dislocation densities, and well-developed intragranular substructures, such as small cell sizes and large sub-grain misorientations. Mean-field crystal plasticity predicts higher Taylor factors for these γ-fiber grains as compared to α-fiber grains, *cf*. Figure 8(a). From a computational standpoint, the pronounced γ-fiber recrystallization texture observed in IF steels (*cf*. Figure 1) is therefore primarily attributed to this stored energy advantage. However, while a high–stored energy criterion successfully explains γ-fiber dominance following conventional cold rolling and annealing, it fails to account for recrystallization textures arising from unconventional rolling paths or modified annealing conditions.

Figure 9 presents two different recrystallization textures of an Fe–1.2 wt pct Si alloy after warm rolling and annealing at 900 °C for 2 hours. Differences between the two textures arise from conventional *vs*. asymmetric rolling configurations. However, a closer look at the Taylor factor maps of Figure 8 challenges a high–stored energy-driven recrystallization mechanism.[46] For examples shown in Figure 9, the dominant components of the recrystallization texture represent orientations with low Taylor factors. In addition to the Rotated Cube, other Cube fiber components and the Goss ($\{110\}\langle001\rangle$) orientation appear in the annealing texture [Figure 9(a)]. These observations indicate that in this case low-energy orientations exhibit higher stability and recrystallization propensity than high-energy counterparts. Consequently, mean-field stored energy simulation alone cannot explain recrystallization texture selection. Additional microstructural factors must be considered.

To study the distinctly different recrystallization textures observed after cold and warm rolling of (extra/ultra-) low-carbon steels, microstructure and texture evolution in IF steel rolled at different temperatures were investigated.[47,48] While deformation textures after cold and warm rolling are similar, EBSD reveals pronounced differences in intragranular substructures. The cold rolled material exhibits significantly higher stored energy, quantified through local misorientation gradients, approximately three times that of the warm-rolled counterpart, together with a broader spatial distribution.[47] These observations demonstrate that local deformation microstructural features, such as sub-grain structure and misorientation heterogeneity, play a critical role in recrystallization and must be incorporated predictive models.

Accordingly, a 2D cellular automaton (CA) sub-grain growth model was employed, using high-resolution EBSD maps as input.[48] Recrystallization is modeled as sub-grain growth driven by boundary migration, with local boundary velocity defined by the product of mobility and a misorientation-dependent driving force derived from the Read–Shockley relation.[49] Despite its relative simplicity, the model successfully captures the preferential development of γ-fiber textures after cold rolling, while predicting Rotated Cube–dominated recrystallization after warm rolling and annealing. Importantly, the simulations emphasize that the observed textures, even in the early stages of recrystallization, are not the result of different recrystallization mechanisms but from one single micro-growth mechanism operating on the initial deformation substructure. These results highlight the decisive role of local crystallographic environments (such as Goss-oriented regions within micro-shear bands, grain boundaries between $\{001\}$ and $\{111\}$ grains or intragranular orientation gradients in and $\{111\}$ grains.

The influence of local misorientation on deformation and recrystallization texture formation in ferritic stainless steels has been further clarified in recent studies.[50,51] In cold rolled material, intragranular misorientation develops in a strongly anisotropic manner, governed by grain orientation, grain shape, and rolling strain, with pronounced orientation-dependent misorientation spreads.[50] On annealing, recrystallization is attributed to competitive sub-grain growth driven by this anisotropy in sub-grain characteristics rather than by differences in average stored energy alone.[51] Incorporating sub-grain-scale descriptors, such as misorientation distributions and sub-grain boundary characteristics, in a mean-field framework yields a recrystallization texture model capable of reproducing the experimentally observed development of the Cube fiber.

IV. SUMMARY

This study examines the formation and evolution of the Cube fiber, with particular emphasis on the Rotated Cube ($\{001\}\langle110\rangle$) component, in extra and ultra low-carbon steels processed *via* conventional flat-sheet. Although conventional rolling and annealing practices are generally unfavorable for Cube fiber development and have historically been optimized to suppress Rotated Cube orientations, experimental evidence demonstrates that this component is continuously present and evolves throughout phase transformation, cold deformation, and recrystallization. During the $\gamma \rightarrow \alpha$ transformation, Rotated Cube ferrite variants naturally arise from Cube oriented austenite through well-established orientation relationships, even in the absence of strong variant selection. Cold rolling further modifies this component, with severe rolling or cross rolling conditions enhancing the Rotated Cube stability far beyond what is predicted by classical crystal plasticity model. Recrystallization introduces additional complexity: while the γ-fiber dominance in conventionally processed steels can be rationalized by nucleation in high stored energy grains, unconventional rolling and annealing conditions reveal recrystallization mechanisms favoring low-energy orientations, including Rotated Cube and related $\alpha^*(\{hh1\}\langle21h\rangle)$-fiber components.

From a modeling perspective, the strengths and limitations of both mean-field and full-field approaches have been assessed. Mean-field crystal plasticity models successfully capture deformation textures at moderate strains but fail to explain the Rotated Cube strengthening at large reductions. The essential development of sub-grain structure caused by grain fragmentation during severe plastic deformation needs to be included in the mean-field CP models for enhancing texture predictions. CA-based recrystallization models, although computationally demanding, demonstrate that sub-grain growth selection based on well-known misorientation mobility differences between low and high angle grain boundaries, in association with Read-Shockley type boundary energy dependence captures the orientation selection in the early stages of recrystallization with reasonable accuracy. The dominant texture components are determined by local microstructural heterogeneity, particularly sub-grain misorientation, boundary character, and shear-band topology. Recent advances incorporating sub-grain descriptors in statistical models are very promising in reconciling computational efficiency with physical fidelity. Overall, the development of the Rotated Cube texture in low-carbon steels emerges as a multiscale phenomenon is critically dependent of the high-resolution features of the deformation microstructure. Progress in Cube texture control will therefore require integrated modeling strategies that explicitly account for phase transformation crystallography, deformation-induced heterogeneity, and sub-grain-scale recrystallization mechanisms within conventional processing routes.

ACKNOWLEDGMENTS

The authors are indebted to Prof. A.D. Rollett (Carnegie Mellon University) for interesting and inspirational discussions on this topic.

CONFLICT OF INTEREST

On behalf of all authors, the corresponding author states that there is no conflict of interest.

REFERENCES

1. Y. He and L.A.I. Kestens: *Int. Mater. Rev.*, 2025, vol. 70, pp. 353–93. https://doi.org/10.1177/09506608251317143.
2. G. Kurdjumow and G. Sachs: *Z. Phys.*, 1930, vol. 64, pp. 325–43.
3. Z. Nishiyama: *Sci. Rep. Tohoku Univ.*, 1934, vol. 23, p. 637.
4. A.B. Greninger and A.R. Troiano: *JOM*, 1949, vol. 1, pp. 590–98.
5. N. Yoshinaga, L.A. Kestens, B.C. De Cooman: $\alpha \rightarrow \gamma \rightarrow \alpha$ transformation texture formation at cold-rolled ultra low carbon steel surfaces. *In Proceedings of the Materials Science Forum*, vol. *495,* Trans Tech Publ, 2005, pp. 1267–72.
6. J. Gautam, R.H. Petrov, and L.A.I. Kestens: *Mater. Sci. Forum*, 2007, vol. 550, pp. 503–08. https://doi.org/10.4028/www.scientific.net/MSF.550.503.
7. J. Gautam, R. Petrov, L. Kestens, and E. Leunis: *J. Mater. Sci.*, 2008, vol. 43, pp. 3969–75. https://doi.org/10.1007/s10853-007-2292-4.
8. P. Gobernado, R. Petrov, D. Ruiz, E. Leunis, and L.A.I. Kestens: *Adv. Eng. Mater.*, 2010, vol. 12, pp. 1077–81. https://doi.org/10.1002/adem.201000075.
9. S. Takajo, C.N. Tomé, S.C. Vogel, and I.J. Beyerlein: *Int. J. Plast.*, 2018, vol. 109, pp. 137–52. https://doi.org/10.1016/j.ijplas.2018.06.001.
10. S. Takajo, S.C. Vogel, and Y. Hayakawa: *ISIJ Int.*, 2019, vol. 59, pp. 541–50. https://doi.org/10.2355/isijinternational.ISIJINT-2018-579.
11. L. Kestens, J.J. Jonas, P. van Houtte, and E. Aernoudt: *Text. Stress Microstruct.*, 1996, vol. 26, p. 260458. https://doi.org/10.1155/TSM.26-27.321.
12. L. Kestens and S. Jacobs: *Text. Stress Microstruct.*, 2008, vol. 2008, p. 173083. https://doi.org/10.1155/2008/173083.
13. H. Homma and B. Hutchinson: *Acta Mater.*, 2003, vol. 51, pp. 3795–3805. https://doi.org/10.1016/S1359-6454(03)00193-9.
14. M. Tomita, T. Inaguma, H. Sakamoto, and K. Ushioda: *ISIJ Int.*, 2016, vol. 56, pp. 693–99. https://doi.org/10.2355/isijinternational.ISIJINT-2015-567.
15. L. Kestens and J.J. Jonas: *Metall. Mater. Trans. A*, 1996, vol. 27A, pp. 155–64. https://doi.org/10.1007/BF02647756.
16. T. Nguyen-Minh, J.J. Sidor, R.H. Petrov, and L.A.I. Kestens: *Scripta Mater.*, 2012, vol. 67, pp. 935–38. https://doi.org/10.1016/j.scriptamat.2012.08.017.
17. M. Mehdi, Y. He, E.J. Hilinski, L.A.I. Kestens, and A. Edrisy: *Acta Mater.*, 2020, vol. 185, pp. 540–54. https://doi.org/10.1016/j.actamat.2019.12.024.
18. Y. Zhi, Y. Jiang, D. Ke, X. Hu, and X. Liu: *Materials*, 2024, vol. 17, p. 1370. https://doi.org/10.3390/ma17061370.
19. A.D. Rollett: *Prog. Mater. Sci.*, 1997, vol. 42, pp. 79–99. https://doi.org/10.1016/S0079-6425(97)00008-X.
20. E.A. Holm, G.N. Hassold, and M.A. Miodownik: *Acta Mater.*, 2001, vol. 49, pp. 2981–91. https://doi.org/10.1016/S1359-6454(01)00207-5.
21. S.R. Kalidindi, C.A. Bronkhorst, and L. Anand: *J. Mech. Phys. Solids*, 1992, vol. 40, pp. 537–69. https://doi.org/10.1016/0022-5096(92)80003-9.
22. F. Roters, M. Diehl, P. Shanthraj, P. Eisenlohr, C. Reuber, S.L. Wong, T. Maiti, A. Ebrahimi, T. Hochrainer, H.O. Fabritius, S. Nikolov, M. Friák, N. Fujita, N. Grilli, K.G.F. Janssens, N. Jia, P.J.J. Kok, D. Ma, F. Meier, E. Werner, M. Stricker, D. Weygand, and D. Raabe: *Comput. Mater. Sci.*, 2019, vol. 158, pp. 420–78. https://doi.org/10.1016/j.commatsci.2018.04.030.
23. R.A. Lebensohn, A.K. Kanjarla, and P. Eisenlohr: *Int. J. Plast.*, 2012, vol. 32–33, pp. 59–69. https://doi.org/10.1016/j.ijplas.2011.12.005.
24. P. Eisenlohr, M. Diehl, R.A. Lebensohn, and F. Roters: *Int. J. Plast.*, 2013, vol. 46, pp. 37–53. https://doi.org/10.1016/j.ijplas.2012.09.012.
25. M. Militzer, M.G. Mecozzi, J. Sietsma, and S. van der Zwaag: *Acta Mater.*, 2006, vol. 54, pp. 3961–72. https://doi.org/10.1016/j.actamat.2006.04.029.
26. C. Zheng and D. Raabe: *Acta Mater.*, 2013, vol. 61, pp. 5504–17. https://doi.org/10.1016/j.actamat.2013.05.040.
27. A. Artemev, Y. Jin, and A.G. Khachaturyan: *Acta Mater.*, 2001, vol. 49, pp. 1165–77. https://doi.org/10.1016/S1359-6454(01)00021-0.
28. Y. Wang and A.G. Khachaturyan: *Mater. Sci. Eng. A*, 2006, vol. 438–440, pp. 55–63. https://doi.org/10.1016/j.msea.2006.04.123.
29. H. Xiang, W. Van Paepegem, and L.A.I. Kestens: *Comput. Mater. Sci.*, 2023, https://doi.org/10.1016/j.commatsci.2023.112067.
30. T. Tomida and M. Wakita: *ISIJ Int.*, 2012, vol. 52, pp. 601–09. https://doi.org/10.2355/isijinternational.52.601.
31. T. Tomida, M. Wakita, M. Yasuyama, S. Sugaya, Y. Tomota, and S.C. Vogel: *Acta Mater.*, 2013, vol. 61, pp. 2828–39. https://doi.org/10.1016/j.actamat.2013.01.015.
32. T. Tomida: *Acta Mater.*, 2018, vol. 146, pp. 25–41. https://doi.org/10.1016/j.actamat.2017.12.033.
33. W.B. Hutchinson, L. Ryde, and P.S. Bate: *Mater. Sci. Forum*, 2005, vol. 495–497, pp. 1141–50. https://doi.org/10.4028/www.scientific.net/MSF.495-497.1141.
34. H. Landheer, S.E. Offerman, R.H. Petrov, and L.A.I. Kestens: *Acta Mater.*, 2009, vol. 57, pp. 1486–96. https://doi.org/10.1016/j.actamat.2008.11.034.

35. B. Hutchinson, L.A.I. Kestens: Origins of texture memory in steels. *In Proceedings of the Applications of Texture Analysis*, 2008, pp. 281–90. https://doi.org/10.1002/9780470444214.ch30.
36. G.I. Taylor: *J. Inst. Metals*, 1938, vol. 62, pp. 307–24.
37. R.A. Lebensohn and C.N. Tomé: *Acta Metall. Mater.*, 1993, vol. 41, pp. 2611–24. https://doi.org/10.1016/0956-7151(93)90130-K.
38. P. Van Houtte, S. Li, M. Seefeldt, and L. Delannay: *Int. J. Plast.*, 2005, vol. 21, pp. 589–624. https://doi.org/10.1016/j.ijplas.2004.04.011.
39. P. Van Houtte: *Mater. Sci. Eng.*, 1982, vol. 55, pp. 69–77. https://doi.org/10.1016/0025-5416(82)90085-4.
40. P. Van Houtte, L. Delannay, and S.R. Kalidindi: *Int. J. Plast.*, 2002, vol. 18, pp. 359–77. https://doi.org/10.1016/S0749-6419(00)00102-9.
41. M. Zecevic, W. Pantleon, R.A. Lebensohn, R.J. McCabe, and M. Knezevic: *Acta Mater.*, 2017, vol. 140, pp. 398–410. https://doi.org/10.1016/j.actamat.2017.08.056.
42. M. Zecevic, R.A. Lebensohn, R.J. McCabe, and M. Knezevic: *Int. J. Plast.*, 2018, vol. 109, pp. 193–211. https://doi.org/10.1016/j.ijplas.2018.06.004.
43. K. Sedighiani, K. Traka, F. Roters, J. Sietsma, D. Raabe, and M. Diehl: *Acta Mater.*, 2022, https://doi.org/10.1016/j.actamat.2022.118167.
44. J. Ochoa-Avendaño, K. Sedighiani, J. Galan-Lopez, C. Bos, and L.A.I. Kestens: *J. Market. Res.*, 2024, vol. 31, pp. 3844–59. https://doi.org/10.1016/j.jmrt.2024.07.030.
45. J.A. Mitchell, F. Abdeljawad, C. Battaile, C. Garcia-Cardona, E.A. Holm, E.R. Homer, J. Madison, T.M. Rodgers, A.P. Thompson, and V. Tikare: *Modell. Simul. Mater. Sci. Eng.*, 2023, vol. 31, p. 055001.
46. T. Nguyen-Minh, R.H. Petrov, S. Cicalè, and L.A.I. Kestens: *JOM*, 2024, vol. 76, pp. 1015–30. https://doi.org/10.1007/s11837-023-06330-3.
47. E. Sepúlveda Hernández, T. Nguyen-Minh, K. Traka, F. Castro Cerda, and L.A.I. Kestens: *Scr. Mater.*, 2024, https://doi.org/10.1016/j.scriptamat.2024.116151.
48. K. Traka, E.S. Hernández, T. Nguyen-Minh, K. Sedighiani, J. Sietsma, and L.A.I. Kestens: *Comput. Mater. Sci.*, 2025, https://doi.org/10.1016/j.commatsci.2024.113425.
49. W.T. Read and W. Shockley: *Phys. Rev.*, 1950, vol. 78, p. 275.
50. A. Després, M. Zecevic, R.A. Lebensohn, J.D. Mithieux, F. Chassagne, and C.W. Sinclair: *Acta Mater.*, 2020, vol. 182, pp. 184–96. https://doi.org/10.1016/j.actamat.2019.10.023.
51. A. Després, J.D. Mithieux, and C.W. Sinclair: *Acta Mater.*, 2021, https://doi.org/10.1016/j.actamat.2021.117226.

Publisher's Note Springer Nature remains neutral with regard to jurisdictional claims in published maps and institutional affiliations.

Springer Nature or its licensor (e.g. a society or other partner) holds exclusive rights to this article under a publishing agreement with the author(s) or other rightsholder(s); author self-archiving of the accepted manuscript version of this article is solely governed by the terms of such publishing agreement and applicable law.